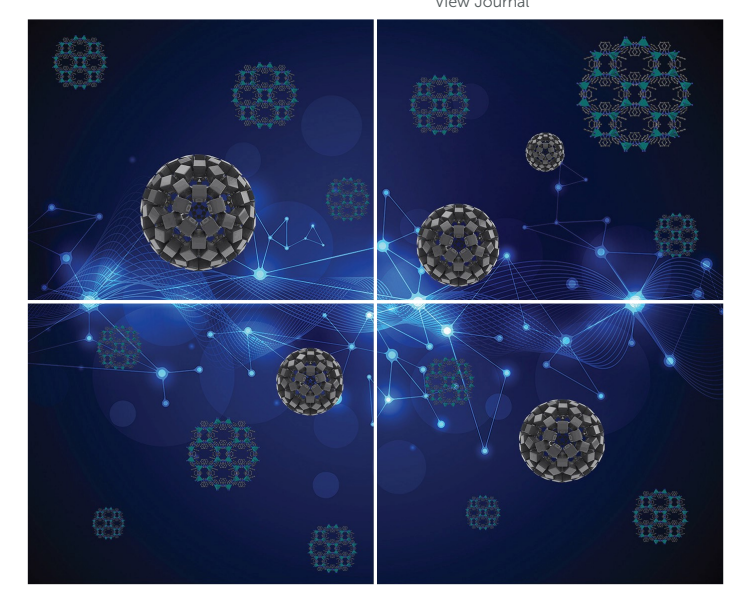
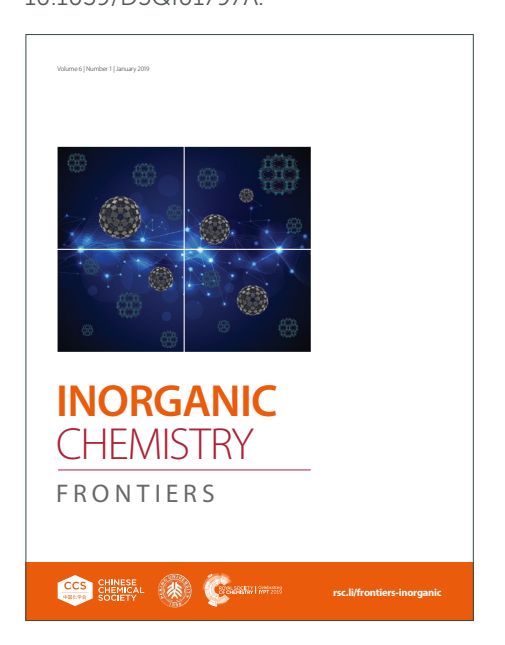
INORGANIC CHEMISTRY

FRONTIERS

Accepted Manuscript



This article can be cited before page numbers have been issued, to do this please use: J. Chen, L. tang, C. Gong, L. Wei, J. Zhang, X. Chen, X. Zhang, Y. Liu, J. Luo and Z. Sun, *Inorg. Chem. Front.*, 2025, DOI: 10.1039/D5QI01797A.



This is an Accepted Manuscript, which has been through the Royal Society of Chemistry peer review process and has been accepted for publication.

Accepted Manuscripts are published online shortly after acceptance, before technical editing, formatting and proof reading. Using this free service, authors can make their results available to the community, in citable form, before we publish the edited article. We will replace this Accepted Manuscript with the edited and formatted Advance Article as soon as it is available.

You can find more information about Accepted Manuscripts in the <u>Information for Authors</u>.

Please note that technical editing may introduce minor changes to the text and/or graphics, which may alter content. The journal's standard <u>Terms & Conditions</u> and the <u>Ethical guidelines</u> still apply. In no event shall the Royal Society of Chemistry be held responsible for any errors or omissions in this Accepted Manuscript or any consequences arising from the use of any information it contains.







Open Access Article. Published on 17 2025. Downloaded on 18.10.25 10:18:55.

View Article Online DOI: 10.1039/D5QI01797A

EDGE ARTICLE

Received 00th January 20xx, Accepted 00th January 20xx

DOI: 10.1039/x0xx000000x

Improper Narrow Bandgap Molecular Ferroelectrics Enable Light-Excited Pyroelectricity for Broadband Self-Powered Photoactivities

Jialu Chen, ^{a, b} Liwei Tang, ^a Chen Gong, ^a Linjie Wei, ^a Jingtian Zhang, ^a Xingguang Chen, ^a Xiaoyu Zhang, ^{a, b} Yi Liu, *a, ^c Junhua Luo, ^{a, c} and Zhihua Sun*a, ^c

Narrow bandgap ferroelectrics are emerging as critical components for assembling high-performance optoelectronic devices with broadband spectral response, yet integrating narrow bandgap and robust ferroelectricity in a single-phase material system remains a huge challenge. Herein, we report a narrow bandgap improper molecular ferroelectric, (DMAPA)Bils (1; DMAPA = dimethylaminopropylammonium), which has the bandgap of 1.94 eV and spontaneous polarization (P_s) value of 1.38 μ C cm⁻². It is notable that 1 exhibits unusual dielectric bistability near its Curie temperature (T_c) = 372 K, along with only quite small variation in dielectric constants. This characteristic of improper ferroelectricity endows 1 with large pyroelectric figures-of-merit. Strikingly, light-induced change of its electric P_s leads to ultraviolet-to-near-infrared pyroelectricity in a wide spectral region (266–980 nm), thus achieving broadband self-powered photoactivities. High-quality thin films of 1 fabricated *via* spin-coating process also exhibit excellent light-induced pyroelectric effects. The integration of photoactivities in narrow bandgap improper ferroelectrics offers a promising pathway toward scalable broadband optoelectronic device application.

Introduction

Ferroelectrics have been developed as an indispensable class of electroactive materials, which are characterized by reversible switching of spontaneous polarization (P_s) under external electric fields. [1-3] The inherent absence of inversion symmetry in ferroelectrics gives rise to a series of coupled physical properties, including pyroelectricity, piezoelectricity, optical nonlinearity. [4,5] These multifunctional properties have a wide range of high-performance electronic and optoelectronic applications, such as piezoelectric sensors, switchable diodes, and self-powered photodetectors. [6,7] In normal ferroelectrics, P_s serves as the primary order parameter during phase transitions. Conversely, for improper ferroelectrics, P_s acts as a secondary order parameter induced by structural distortions, spin ordering, or charge ordering. [8-10] Improper ferroelectrics usually show small variation in dielectric constants near Curie temperature (T_c) , values consistently at least an order of magnitude lower than those of proper ferroelectrics.^[11,12] Dielectric bistability refers to switchable dielectric states, characterized by the presence of two

Recently, organic–inorganic hybrid perovskites (OIHPs) have emerged as a versatile platform for the development of new ferroelectric materials with tunable optical and electronic properties. [17,18] OIHPs formed through chemical self-assembly of inorganic metal-halogen frameworks and organic cations. [19] These architectures combine the design flexibility and solution processability of organic molecules with the functional robustness of inorganic networks. [20] The inorganic metal-halide frameworks play a dominant role in determining the energy band structure. [21,22] Thus, the engineering of metal and halide composition (e.g., CI, Br, I) can effectively tailor the band edge positions and optical bandgap. [23,24] Simultaneously, the incorporation of polar organic

stable phases that remain nearly temperature-invariant during phase transitions. The relatively small dielectric constants values may indicate the presence of improper ferroelectricity, thereby enabling dramatic pyroelectric figures of merit (FOMs) or lightpyroelectricity.[13] Conventional inorganic oxide ferroelectrics such as PbTiO₃, PbZrO₃, and NaNbO₃, typically possess wide bandgaps (3.5-4.1 eV),[14] limiting their ability to harvest solar energy efficiently across the visible and near-infrared (NIR) spectra. Although ferroelectric materials with narrow bandgaps are highly desirable for applications such as broadband photodetection and solar-powered energy harvesting, [15] the associated increase in leakage current often compromises polarization stability and deteriorates ferroelectric performances.[16] Therefore, realizing the coexistence of narrow bandgap and stable ferroelectricity is a crucial bottleneck in the development of multifunctional optoelectronic materials.

^{a.} State Key Laboratory of Functional Crystals and Devices, Fujian Institute of Research on the Structure of Matter, Chinese Academy of Sciences, Fuzhou, Fujian 350002, China

E-mail: sunzhihua@fjirsm.ac.cn

b. College of Chemistry and Materials Science, Fujian Normal University, Fuzhou

^c Fujian College, University of Chinese Academy of Sciences, Fuzhou 350000, China

ganic Chemistry Frontiers Accepted Manu

ARTICLE Journal Name

cations can induce lattice distortions that support ferroelectric behavior, yielding both efficient light absorption and polarization switching capability.^[25,26] This unique combination establishes OIHPs as promising optoelectronic candidates, positioning them as cornerstone architectures for new molecular ferroelectric systems.

As the emerging ferroelectric subclass of OIHPs, the bismuth (Bi)-based alternatives have attracted increasing attention due to their flexible electronic structures and superior environmental compatibility. [27-37] In this work, we have developed a new Bi-based molecular ferroelectric with the narrow bandgap (~1.94 eV), (DMAPA)Bil₅ (1), which exhibits bistable dielectricity and improper ferroelectricity. Strikingly, light-induced pyroelectricity in the ultraviolet (UV)-to-near-infrared (NIR) spectral region achieve broadband self-powered photoactivity. The successful fabrication of high-quality thin films further highlights its potential for scalable integration into advanced optoelectronic systems.

Results and Discussion

Variable-Temperature Structure Analyses

High-quality red-black crystals of 1 were obtained by slowly cooling its solution in HI, as depicted in Figure 1a.19He3powdelX-7ay diffraction (XRD) results match well with the simulated pattern, verifying the phase purity of 1 as well as its phase stability over 120 days (Figure S1). Thermogravimetric analysis (TGA) indicates that 1 can be thermally stable up to 571 K without any thermal decomposition (Figure S2). To elucidate structural features and correlate them with functional properties, single crystal X-ray diffraction analysis was performed. At 273 K, 1 crystallizes in the monoclinic chiral space group P2₁. The basic structure adopts a 1D chain-like topology spiraling along the a-axis, composed of organic cations and extended inorganic framework chains formed by the face sharing Bil₆ octahedra (Figure 1c). Since an ideal octahedron requires uniform bond lengths and angles, 1 exhibits stereochemical geometry distortion characterized by bond length variations (2.961-3.351 Å) and angular deviations (167.25°-171.58°), as quantified in Figure S3 and Table S3. Each organic (DMAPA)2+ cation contributes two fully protonated ammonium groups, with N-H···I hydrogen bonds anchoring the inorganic chains (Figure 1b).

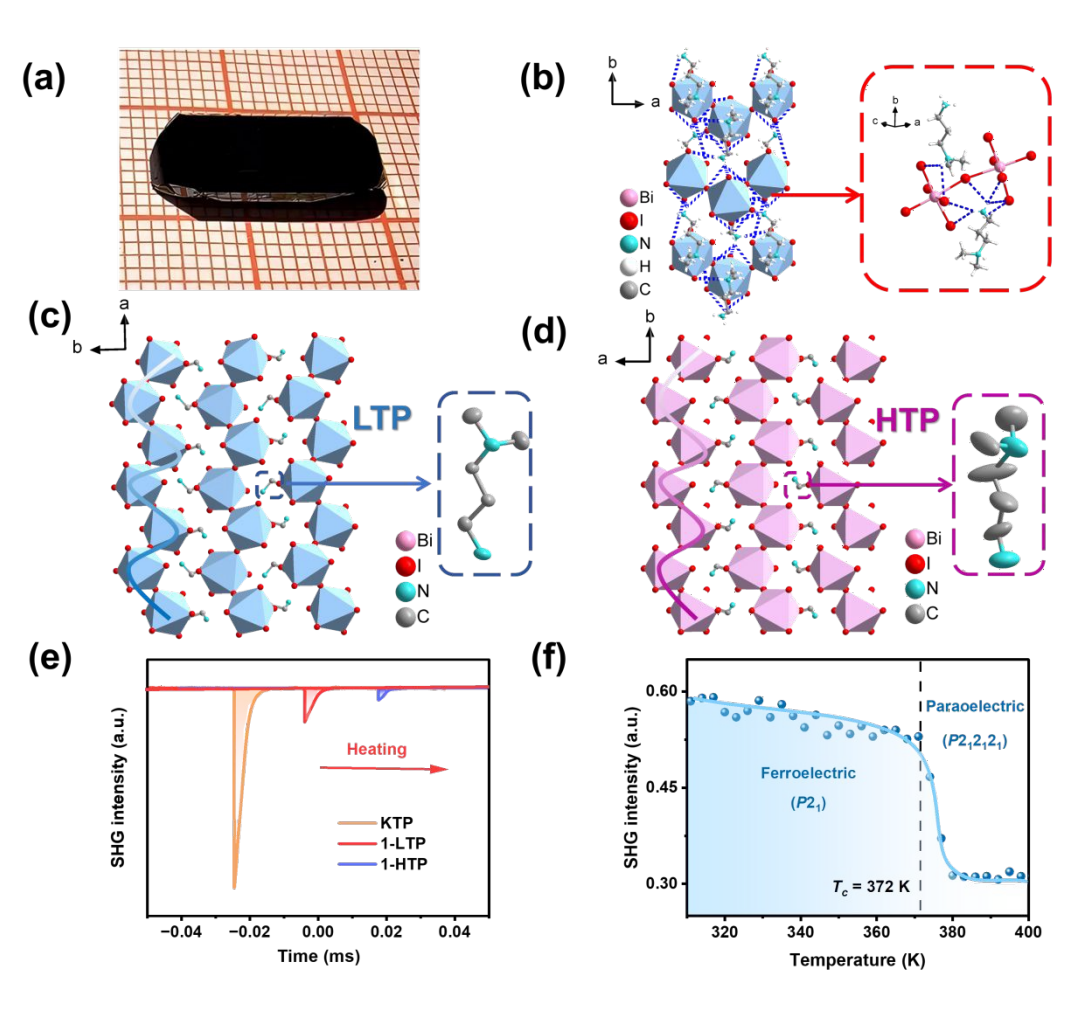


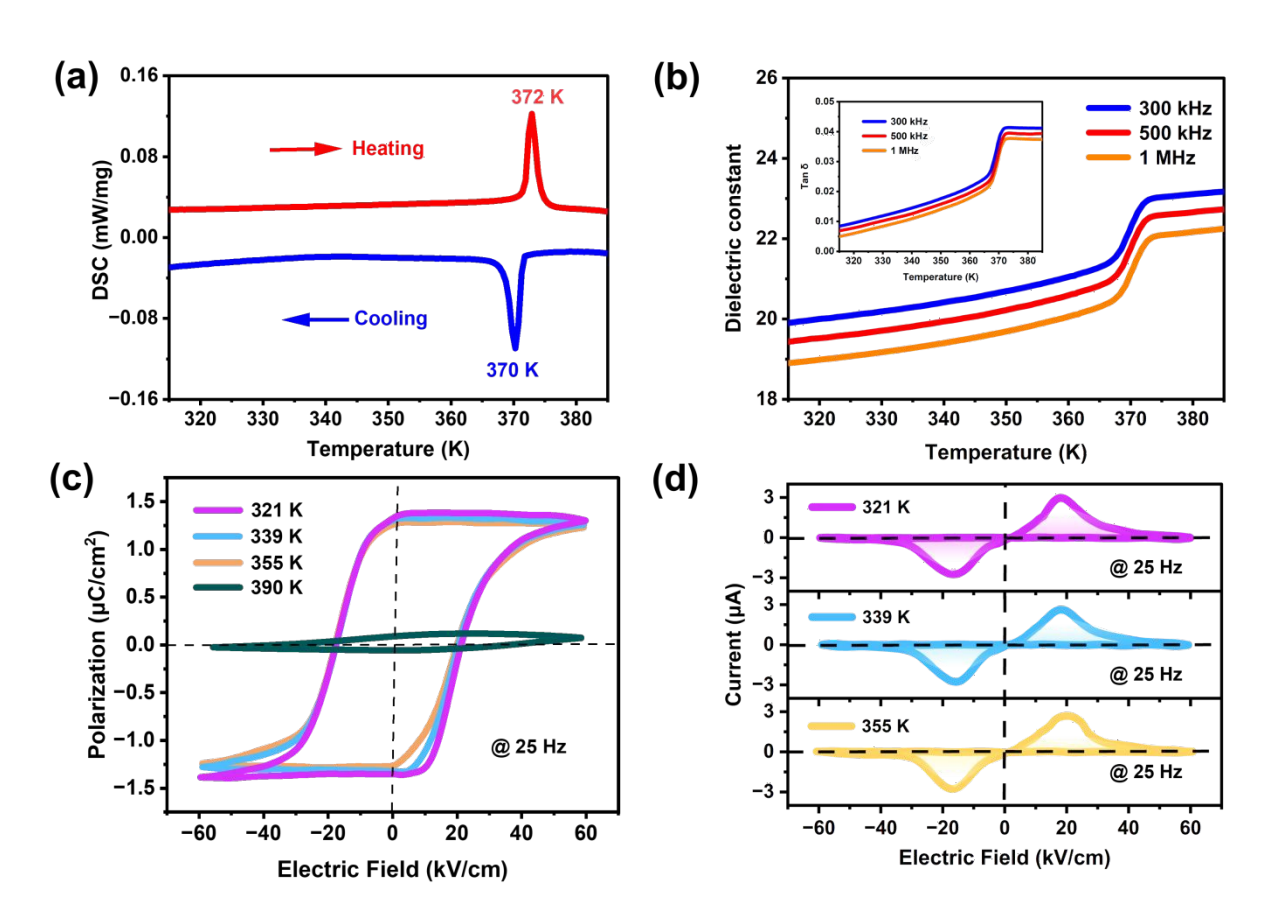
Fig. 1 Crystal structures of **1** at different phases. a) Bulk crystal obtained by the temperature-cooling method. b) The N-H···l hydrogenbonding interactions between organic cations and inorganic frameworks at 273 K. c) Packing diagram as viewed in the direction of the *c*-axis at 273 K (ferroelectric phase, FEP). The small cation configuration at ferroelectric phase is highlighted within the blue rectangle. (d) Packing structure observed at 400 K (paraelectric phase, PEP). e) The comparison of SHG signals of **1** and KDP. f) Variable-temperature SHG intensities.

Two adjacent cations parallel to the α -axis exhibit mutual tilting at a specific angle. Structurally, the directional alignment of organic cations combined with Bil6 octahedral tilting facilitates electric polarization. The high-temperature phase (HTP) of 1 crystallizes in the nonpolar orthorhombic space group P2₁2₁2₁. Organic cations display significantly expanded thermal ellipsoids compared to the low-temperature phase (LTP), indicating an order-disordered transformation (Figure 1d). Furthermore, variable-temperature second harmonic generation (SHG) served as an effective technique for symmetry breaking across the phase transition (Figure 1e). At the LTP, the SHG signal exhibits a sharp intensity, approximately 0.2 times that of KH₂PO₄ (KDP), confirms that 1 crystallizes in a noncentrosymmetric space group at room temperature. Upon heating, the SHG signals display an abrupt decrease above T_c , with the intensity reduced to approximately 0.1 times that of KDP (Figure 1f). This result unambiguously confirms that 1 undergoes a phase transition and that the space group P2₁2₁2₁ is consistent with its noncentrosymmetric structure in the HTP. This process corresponds to the symmetry breaking characterized by Aizu notation 222F2.[1,38] The number of symmetric elements reduces from 4 (E, C2, C2', C2") to 2 (E, C2), consistent with Landau phase transition theory (Figure S4). In this context, the ferroelectric phase transition of 1 represents a temperature-driven order-disorder transition driven by molecular motion of (DMAPA)²⁺ cations.

Ferroelectric and Phase Transition Properties

The structural changes of 1 are closely correlated with its phase transition behavior, preliminarily confirmed byodifferentials scanning calorimetry (DSC) measurements. As shown in Figure 2a, a pair of endothermic/exothermic peaks at 372/370 K are clearly observed during heating and cooling processes, indicating a reversible phase transition in 1. Specific heat capacity (C_p) measurement further corroborates this transition (Figure S5). Besides, distinct step-like dielectric anomalies are also observed nearby 372 K, as depicted in **Figure 2b**. The dielectric constant (ε_r) of **1** displays a very small change from 20 to 23 at 300 kHz during the phase transition, and two stable dielectric plateaus are observed upon heating. 1 exhibits minimal dielectric loss ($tan\delta$) variation from 0.008 to 0.04 at 300 kHz near its T_c (Figure 2b). The minimal temperature-dependent variations in dielectric constant and dielectric loss across broad thermal ranges hints the improper ferroelectric characteristics of Such temperature-dependent properties demonstrate dielectric bistability in $\mathbf{1}$, where P_{s} functions as a secondary order parameter of improper ferroelectrics. It is proposed that exploiting dielectric bistability in improper ferroelectrics provides an effective strategy for optimizing pyroelectric FOMs.

The definitive characteristic of ferroelectric materials is the reversible switching of P_s direction under applied external electric fields.^[40] This can be verified through polarization-electric field (*P-E*)



This article is licensed under a Creative Commons Attribution-NonCommercial 3.0 Unported Licence

Open Access Article. Published on 17 2025. Downloaded on 18.10.25 10:18:55.

ARTICLE Journal Name

Fig. 2 Structural phase transition and related physical properties of 1. a) DSC curves measured upon heating and cooling. b), Temperature dependence of the dielectric constant. Inset: the corresponding dielectric loss. c) P-E hysteresis loops obtained at different temperatures (from the dielectric constant). = 25 Hz). d) The current loop of 1 measured at different temperatures (f = 25 Hz).

hysteresis loop measurement. As illustrated in Figure 2c, the well defined P-E hysteresis loops measured at different temperatures provide solid evidence for the ferroelectricity in 1. At 321 K, the P-E loop gives its P_s value of approximately ~1.4 μ C cm⁻² and coercive field (E_c) of ~17 kV cm⁻¹, significantly lower than those of inorganic ferroelectric BaTiO₃ ($E_c = 30 \text{ kV cm}^{-1}$) and polymer PVDF ($E_c = 500 \text{ kV}$ cm⁻¹). $^{[41,42]}$ When the temperature exceeds its T_c (372 K), the remnant polarization drops to zero, and ${\bf 1}$ transform to the paraelectric phase. The two opposing current peaks in the currentvoltage (J-E) curves at various temperatures also serve as the conclusive evidence of ferroelectricity in 1 (Figure 2d).

Band Gap Calculation Theory and Comparative Analysis

To investigate optical properties of 1, the UV-vis absorption spectrum was measured at room temperature. As shown in Figure 3a, the spectrum exhibits a strong absorption onset at the band edge (639 nm). By analyzing the power law dependence of the absorption coefficient on photon energy (inset of Figure 3a), the bandgap was determined to be 1.94 eV. The bandgap value obtained from first-principles band structure calculations is 1.86 eV (Figure 3b), being consistent with experimentally determined result. PDOS analysis reveals that the valence band maximum (VBM) and conduction band minimum (CBM) at the G-point are primarily constituted by I-5p and Bi-6p orbitals (Figure 3c). This finding underscores the decisive role of the inorganic framework in modulating the bandgap and electronic structure. Notably, bandgap of 1 remains relatively narrow among known ferroelectrics (Figure 3d).[43-48] The core advantage of narrow bandgap molecular

ferroelectrics lies in their broadened spectral response range, which manifests pronounced light-induced pyroelectric effects via synergistic interplay with the ferroelectric polarization field. [49]

Pyroelectric Effect and Broadband Photoinduced Response

Subsequently, we investigated the pyroelectric properties of 1 using single crystals, which demonstrate a sharp pyroelectric current arising from charge displacement near the T_c (Figure 4a). The temperature dependence of polarization obtained through pyroelectric measurements gives the Ps value of approximately 1.4 μC cm⁻². As another important parameter, the pyroelectric coefficient (p_e , i.e., $|\partial P_s/\partial T|$) is also estimated to be 2.5 × 10⁻³ μ C·cm⁻²·K⁻¹ at room temperature, which rises to 0.64 μ C·cm⁻²·K⁻¹ near T_c (Figure S6). The room-temperature value is smaller than those of conventional pyroelectric materials, such as triglycine sulfate (TGS, $p_e \approx 5.5 \times 10^{-2} \ \mu \text{C} \cdot \text{cm}^{-2} \cdot \text{K}^{-1}$) and $Ba_{0.85}Ca_{0.15}Zr_{0.1}Ti_{0.9}O_3$ (BZT, $p_e \approx 9.8 \times 10^{-2} \, \mu \text{C} \cdot \text{cm}^{-2} \cdot \text{K}^{-1}$). [50,51] For pyroelectric detection two key pyroelectric FOMs are voltage responsivity $F_V = p_e/(\varepsilon_0 \varepsilon_r c_v)$ and detectivity $F_D = p_e/[c_v(\varepsilon_0\varepsilon_r \tan\delta)^{1/2}]$, where ε_0 denotes vacuum permittivity, c_v represents volumetric heat capacity, and $tan\delta$ is dielectric loss. These FOMs quantify maximum pyroelectric voltage per energy input and weak-signal detection capability, respectively. [52] At room temperature, the F_V and F_D values of ${\bf 1}$ are estimated as $\sim 3.0 \times 10^{-4} \text{ cm}^2 \mu\text{C}^{-1}$ and $\sim 1.24 \times 10^{-5} \text{ Pa}^{-1/2}$, respectively. Owing to its improper ferroelectric, 1 exhibits significantly reduced and $tan\delta$ compared

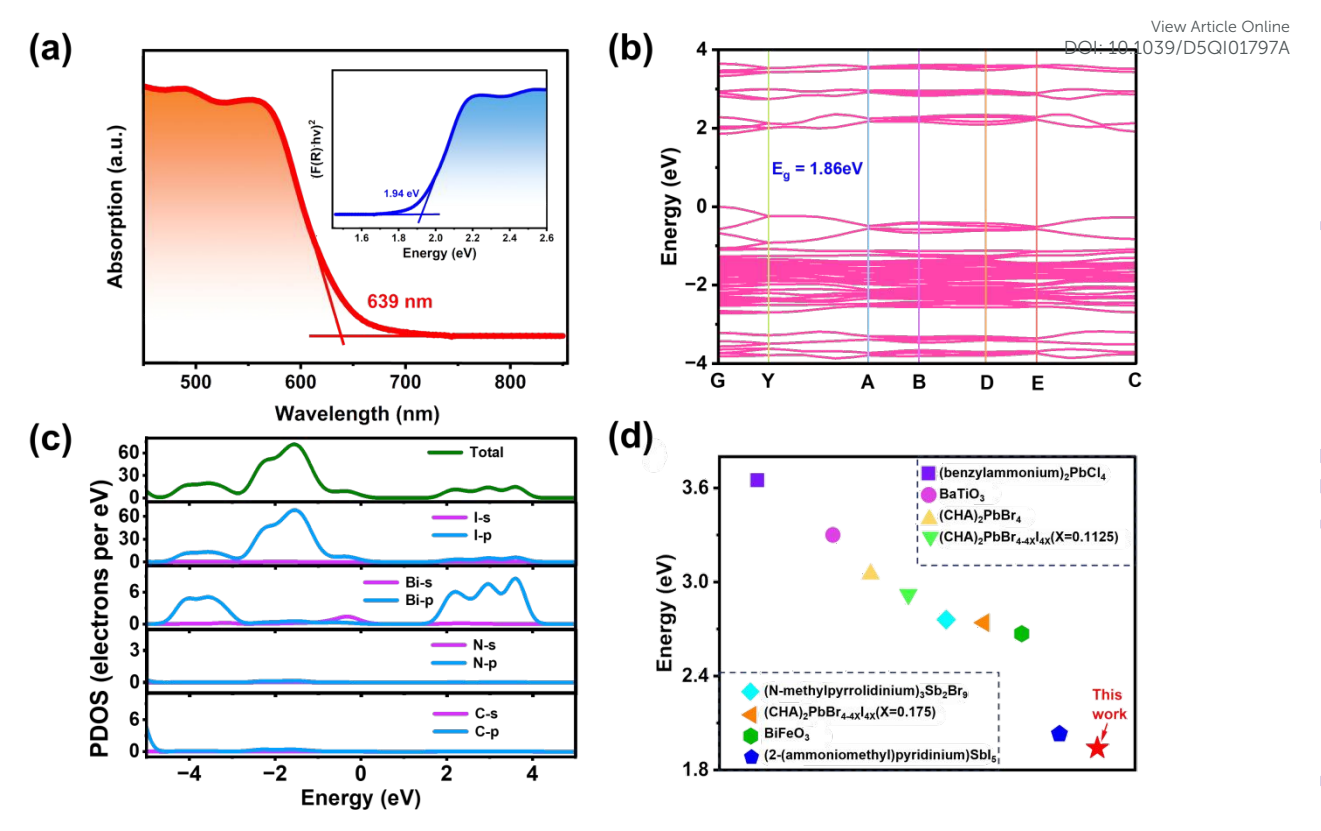


Fig. 3 a) UV-vis absorption spectra of **1**. Inset: the corresponding *Tauc* plot. b) Calculated band structure and c) PDOS spectra near the Fermi level. d) Bandgap comparison of **1** and several typical ferroelectrics.

ARTICLE Journal Name

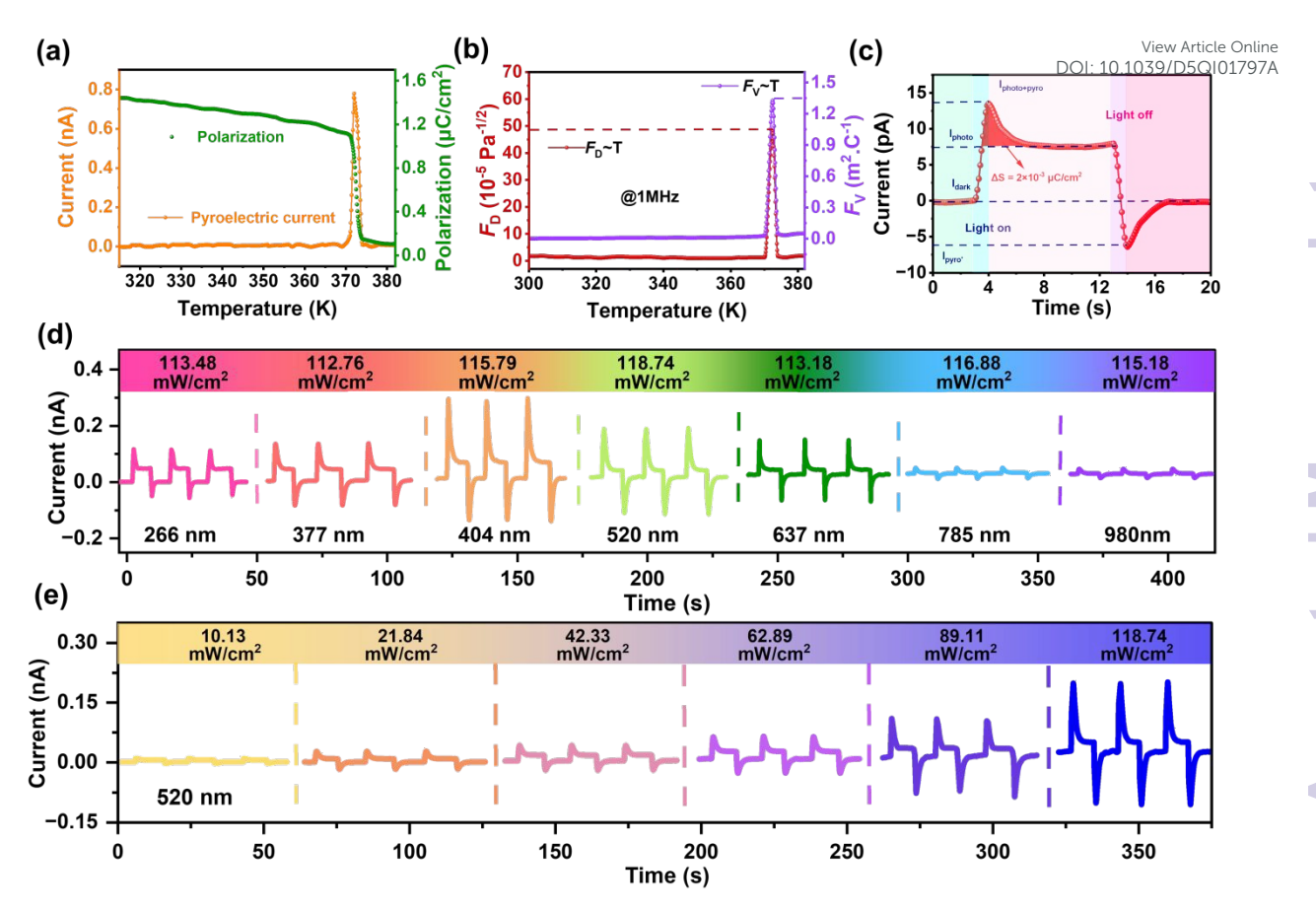


Fig. 4 a) Temperature-dependent pyroelectric currents and P_S deduced by integrating pyroelectric current. b) The simulated two FOMs of F_V and F_D . c) I-t curves measured under 404 nm irradiation at zero bias (5.44 mW cm⁻²). d) Photoactivities of **1** under light illumination of different wavelengths. e) I-t curves measured under 520 nm laser irradiation with different densities at zero bias.

proper ferroelectric counterparts. This results in a dramatic enhancement of the pyroelectric FOMs in the vicinity of the $T_{\rm c}$ (Figure 4b).

To further study photosensitivity, light-induced pyroelectric measurements were performed at room temperature. Taking the 404 nm laser (5.44 mW cm⁻²) as example, the abrupt temperature increase at the crystal surface upon illumination reduces the polarization. This process disrupts the initial alignment of electric dipoles and generates a positive pyroelectric current. Under continuous illumination, the stabilization of temperature correlates with a steady photovoltaic current plateau. Upon light termination, the sudden surface cooling induces polarization variation that produces a transient pyroelectric current with opposite direction, which rapidly decays to the dark state during prolonged darkness (Figure 4c). Thermal equilibrium analysis reveals an integrated charge of 2 \times $10^{-3}~\mu C$ cm^{-2} over the temperature-rise fluctuation (red region, Figures 4c and S7), yielding the $p_{\rm e}$ of 2.33 \times 10⁻³ μ C cm⁻² K⁻¹ at this irradiance. This value coincides with that obtained from the pyroelectric measurement.

Figure 4d displays light-induced pyroelectric currents measured along the polar b-axis under different wavelengths. For incident

light with wavelengths below the bandgap (266-637 nm), transient pyroelectric current (I_{pyro}) and steady photovoltaic current (I_{photo}) coexist. This coupling exhibits strong wavelength dependence, with maximum output emerging near 404 nm. Under above bandgap wavelength irradiation, the attenuated I_{photo} nearly vanishes at photon energies far below the bandgap since low-energy photons cannot directly excite charge carrier migration in 1. However, distinct transient Ipyro peaks persist across a broad ultraviolet-toinfrared spectral range (up to 980 nm). The measured currents at exhibit wavelength-dependent radiation intensity characteristics, which gradually decrease with the increasing wavelength. Figure 4e shows the corresponding current-time (I-t) curves under 520 nm laser irradiation at zero bias. With increasing incident power, the I_{pyro} peaks intensify significantly and demonstrate the intensity-dependent behaviors. These results confirm that the coupling of photovoltaic I_{photo} and light-induced I_{pyro} would enhance photoresponsivity. In addition, photostability measurement at 404 nm (115.79 mW cm⁻²) shows stable transient photopyroelectric outputs over multiple cycles without degradation (Figure S8). Crystalline devices retain approximately 100% initial performance after two-month ambient exposure (115.79 mW cm⁻², Figure S9), demonstrating exceptional stability for practical application. Critically, all properties of 1 are achieved without

This article is licensed under a Creative Commons Attribution-NonCommercial 3.0 Unported Licence.

Open Access Article. Published on 17 2025. Downloaded on 18.10.25 10:18:55.

Journal Name ARTICLE

external power (at zero bias), which establish these polarization-directed characteristics as a promising platform for broadband photoactivity, particularly in self-powered photodetection.

Thin Film Characterization and Photoinduced Pyroelectric Effects

Another striking feature is that 1 can be easily deposited on flexible plastic substrates via spin-coating. The films exhibit uniform red transparent surfaces (Figure 5a) devoid of visible pinholes, indicative of high crystallite distribution. Scanning electron microscopy (SEM) image also confirms this conclusion (Figure S10). The structure of the thin film is verified by XRD measurements, which shows good crystallinity and phase purity (Figure 5b). Figure **5c** presents the height topography image of the ferroelectric thin film acquired through atomic force microscopy (AFM). The AFM analysis reveals that the spin-coated film exhibits complete substrate coverage and exceptional surface uniformity, demonstrating nanoscale flatness with a root mean square roughness of 3.68 nm. Profilometry measurements reveal the film thickness of 107.05 nm and surface roughness of 3.92 nm (Figure S11). This corroborates superior film continuity, where ultra-low defect density enables efficient charge transport and rapid response kinetics.^[53] Further, thin films devices were fabricated by

sputtering gold electrodes on the surface of high-quality thin films (Figure 5d). As shown in Figure 5e, under 2001 high 300 2007 high laser illumination, the characteristic four-stage photoresponse behavior of the current over time is clearly observed, where the peak photocurrent gradually increases with higher incident light intensities. The consistency in response between thin-film and single-crystalline devices highlights the light-induced pyroelectric properties of 1 across different morphologies.

Conclusion

In summary, we have reported a molecular ferroelectric material, (DMAPA)Bil $_{5}$, that combines the narrow bandgap (1.94 eV) with excellent ferroelectricity. Furthermore, the improper ferroelectric nature of ${\bf 1}$ endows it with a large pyroelectric FOMs with the F_{V} and F_{D} peaks far exceeding those of conventional ferroelectric materials. Critically, ${\bf 1}$ not only achieves broadband (266-980 nm) self-powered photoactivities in single-crystalline form but also demonstrates exceptional light-induced pyroelectric effects in thin-film devices. This study marks a critical step forward for molecular ferroelectrics, overcoming long-standing material morphology limitations while opening new avenues for autonomous optoelectronic device engineering.

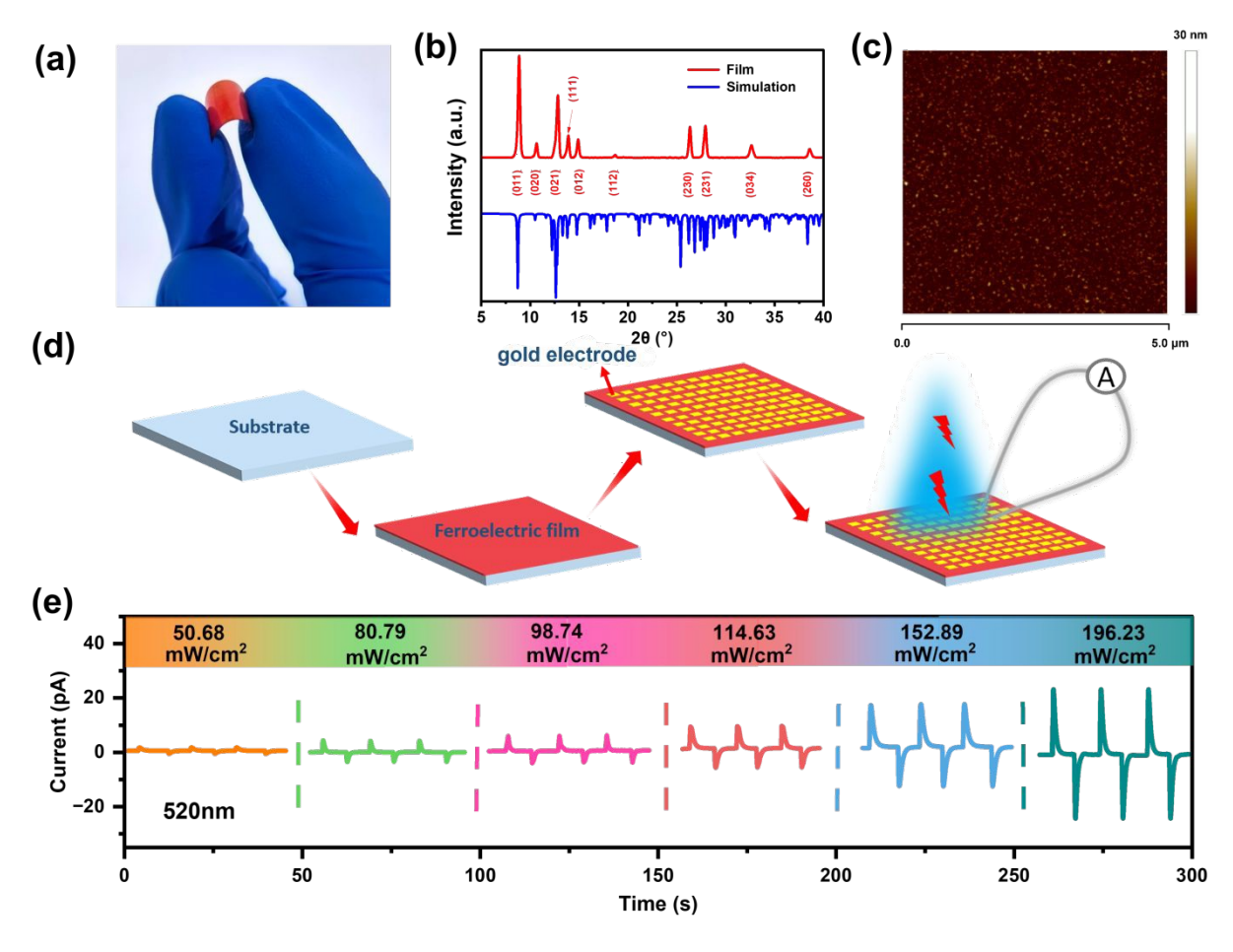


Fig. 5 a) Image of the flexible ferroelectric film of **1**. b) XRD patterns of the ferroelectric film based on the substrate platform and theoretical data. c) AFM image of the thin film of **1**. d) Schematic diagram of the thin-film device fabrication process. e) *I–t* curves measured under 520 nm laser irradiation with different densities at zero bias.

Open Access Article. Published on 17 2025. Downloaded on 18.10.25 10:18:55.

This article is licensed under a Creative Commons Attribution-NonCommercial 3.0 Unported Licence

[CCDC 2471887 and 2471892 contain the supplementary crystallographic data for this paper. These data can be obtained free of charge from The Cambridge Crystallographic Data Centre via www.ccdc.cam.ac.uk/data_request/cif.]

Author contributions

Jialu Chen wrote the manuscript; Liwei Tang and Chen Gong performed the data analysis; Linjie Wei and Jingtian Zhang performed the validation; Xingguuang Chen and Xiaoyu Zhang performed the data curation; Yi Liu performed the methodology; Junhua Luo and Zhihua Sun reviewed this article.

Conflicts of interest

The authors declare no conflict of interest.

Data availability

The data supporting the findings of this study are available within the SI.

Acknowledgements

This work is supported by NSFC (22125110, U23A2094, 22205233, 22305248 and U21A2069), the Natural Science Foundation of Fujian Province (2023J02028 and 2025J01247), the Fujian Science & Technology Innovation Laboratory for Optoelectronic Information of China (2021ZR126), the Postdoctoral Fellowship Program of CPSF under Grant Number (GZB20240746), and the China Postdoctoral Science Foundation (2024T170923 and 2024M753233).

References

- Shi, P.-P.; Tang, Y.-Y.; Li, P.-F.; Liao, W.-Q.; Wang, Z.-X.; Ye, Q.; Xiong, R.-G. Symmetry Breaking in Molecular Ferroelectrics. Chem. Soc. Rev. 2016, 45 (14), 3811–3827.
- Liu, J.; Su, L.; Zhang, X.; Shtansky, D. V.; Fang, X. Ferroelectric— Optoelectronic Hybrid System for Photodetection. Small Methods 2024, 8 (2), 2300319.
- Gao, P.; Nelson, C. T.; Jokisaari, J. R.; Baek, S.-H.; Bark, C. W.; Zhang, Y.; Wang, E.; Schlom, D. G.; Eom, C.-B.; Pan, X. Revealing the Role of Defects in Ferroelectric Switching with Atomic Resolution. *Nat. Commun.* 2011, 2 (1), 591.
- Li, W.; Ma, Y.; Liu, Y.; Fan, Q.; Xu, H.; Guo, W.; Tang, L.; Rong, H.; Sun, Z.; Luo, J. Zipper-Like Dynamic Switching of Coordination Bonds Gives a Polar Bimetallic Halide Toward Self-Driven X-Ray Detection. *Angew. Chem. Int. Ed.* 2025, 64 (4), e202417036.
- Xu, W.-J.; Kopyl, S.; Kholkin, A.; Rocha, J. Hybrid Organic-Inorganic Perovskites: Polar Properties and Applications. Coordin. Chem. Rev. 2019, 387, 398–414.
- 6. Paillard, C.; Bai, X.; Infante, I. C.; Guennou, M.; Geneste, G.;
 Alexe, M.; Kreisel, J.; Dkhil, B. Photovoltaics with

- Ferroelectrics: Current Status and Beyond. *Adv. Mater.* **2016**, View Article Online 28 (26), 5153–5168. DOI: 10.1039/D5QI01797A
- 7. Park, I.-H.; Kwon, K. C.; Zhu, Z.; Wu, X.; Li, R.; Xu, Q.-H.; Loh, K. P. Self-Powered Photodetector Using Two-Dimensional Ferroelectric Dion–Jacobson Hybrid Perovskites. *J. Am. Chem. Soc.* **2020**, *142* (43), 18592–18598.
- Dvořák, V. Improper Ferroelectrics. Ferroelectrics 1974, 7 (1), 1–
 9.
- Benedek, N. A.; Fennie, C. J. Hybrid Improper Ferroelectricity: A Mechanism for Controllable Polarization-Magnetization Coupling. *Phys. Rev. Lett.* 2011, 106 (10), 107204.
- 10. Sun, Z.; Tang, Y.; Zhang, S.; Ji, C.; Chen, T.; Luo, J. Ultrahigh Pyroelectric Figures of Merit Associated with Distinct Bistable Dielectric Phase Transition in a New Molecular Compound: Din -Butylaminium Trifluoroacetate. Adv. Mater. 2015, 27 (32), 4795–4801.
- Guo, L.; Liu, X.; Gao, L.; Wang, X.; Zhao, L.; Zhang, W.; Wang, S.; Pan, C.; Yang, Z. Ferro-Pyro-Phototronic Effect in Monocrystalline 2D Ferroelectric Perovskite for High-Sensitive, Self-Powered, and Stable Ultraviolet Photodetector. ACS Nano 2022, 16 (1), 1280–1290.
- 12. Ma, Y.; Wang, J.; Guo, W.; Han, S.; Xu, J.; Liu, Y.; Lu, L.; Xie, Z.; Luo, J.; Sun, Z. The First Improper Ferroelectric of 2D Multilayered Hybrid Perovskite Enabling Strong Tunable Polarization-Directed Second Harmonic Generation Effect. Adv. Funct. Mater. 2021, 31 (37), 2103012.
- 13. Hua, L.; Wang, J.; Liu, Y.; Guo, W.; Ma, Y.; Xu, H.; Han, S.; Luo, J.; Sun, Z. Improper High- T_c Perovskite Ferroelectric with Dielectric Bistability Enables Broadband Ultraviolet-to-Infrared Photopyroelectric Effects. Adv. Sci. 2023, 10 (19), 2301064.
- 14. Scott, J. F. Applications of Modern Ferroelectrics. *Science* **2007**, *315* (5814), 954–959.
- 15. Nechache, R.; Harnagea, C.; Li, S.; Cardenas, L.; Huang, W.; Chakrabartty, J.; Rosei, F. Bandgap Tuning of Multiferroic Oxide Solar Cells. *Nat. Photonics* **2015**, *9* (1), 61–67.
- Zhang, H.; Wei, Z.; Li, P.; Tang, Y.; Liao, W.; Ye, H.; Cai, H.; Xiong, R. The Narrowest Band Gap Ever Observed in Molecular Ferroelectrics: Hexane-1,6-diammonium Pentaiodobismuth(III). Angew. Chem. Int. Ed. 2018, 57 (2), 526–530.
- Shen, Y.; Ran, C.; Dong, X.; Wu, Z.; Huang, W. Dimensionality Engineering of Organic-Inorganic Halide Perovskites for Next-Generation X-Ray Detector. Small 2024, 20 (16), 2308242.
- Liu, M.; Zhang, H.; Gedamu, D.; Fourmont, P.; Rekola, H.; Hiltunen, A.; Cloutier, S. G.; Nechache, R.; Priimagi, A.; Vivo, P. Halide Perovskite Nanocrystals for Next-Generation Optoelectronics. Small 2019, 15 (28), 1900801.
- 19. Liu, Y. Research Progress on Structure and Property of Hybrid Organic-Inorganic Perovskite. *IOP Conf. Ser.: Earth Environ. Sci.* **2021**, *781* (2), 022069.
- Gao, Y.; Shi, E.; Deng, S.; Shiring, S. B.; Snaider, J. M.; Liang, C.; Yuan, B.; Song, R.; Janke, S. M.; Liebman-Peláez, A.; Yoo, P.; Zeller, M.; Boudouris, B. W.; Liao, P.; Zhu, C.; Blum, V.; Yu, Y.; Savoie, B. M.; Huang, L.; Dou, L. Molecular Engineering of

Journal Name ARTICLE

- Organic-Inorganic Hybrid Perovskites Quantum Wells. *Nat. Chem.* **2019**, *11* (12), 1151–1157.
- Deng, Z.; Ma, J.; Peng, Y.; Yao, Y.; Chang, Y.; Qin, N.; Jia, J.; He, R.; Zhou, L.; Li, M. Embedding Te(IV) into a Robust Sn(IV)-Based Metal Halide for Deep-Red Emission. *Inorg. Chem.* 2025, 64 (8), 4103–4112.
- 22. Li, Q.; Li, S.; Wang, K.; Quan, Z.; Meng, Y.; Zou, B. High-Pressure Study of Perovskite-Like Organometal Halide: Band-Gap Narrowing and Structural Evolution of [NH₃-(CH₂)₄-NH₃]CuCl₄. *J. Phys. Chem. Lett.* **2017**, *8* (2), 500–506.
- 23. Lin, C.; Zhao, Y.; Liu, Y.; Zhang, W.; Shao, C.; Yang, Z. The Bandgap Regulation and Optical Properties of Alloyed Cs²NaSbX⁶ (X=Cl, Br, I) Systems with First Principle Method. *J. Mater. Res. Technol.* 2021, 11, 1645–1653.
- Slavney, A. H.; Leppert, L.; Saldivar Valdes, A.; Bartesaghi, D.; Savenije, T. J.; Neaton, J. B.; Karunadasa, H. I. Small-Band-Gap Halide Double Perovskites. *Angew. Chem. Int. Ed.* 2018, 57 (39), 12765–12770
- 25. Hautzinger, M. P.; Mihalyi-Koch, W.; Jin, S. A-Site Cation Chemistry in Halide Perovskites. *Chem. Mater.* **2024**, *36* (21), 10408–10420.
- Wu, F.; Li, X.; Pan, D.; Sun, Z.; Luo, J.; Liu, X. Geometrical Designing of a Soft-Layered Halide Perovskite Improper Photoferroelectric for Boosted Photostriction. Adv. Opt. Mater. 2023, 11 (23), 2300967.
- Chen, X.; Jia, M.; Xu, W.; Pan, G.; Zhu, J.; Tian, Y.; Wu, D.; Li, X.;
 Shi, Z. Recent Progress and Challenges of Bismuth-Based Halide Perovskites for Emerging Optoelectronic Applications. Adv. Opt. Mater. 2023, 11 (3), 2202153.
- Sun, Z.; Zeb, A.; Liu, S.; Ji, C.; Khan, T.; Li, L.; Hong, M.; Luo, J. Exploring a Lead-free Semiconducting Hybrid Ferroelectric with a Zero-Dimensional Perovskite-like Structure. *Angew. Chem.* 2016, 128 (39), 12033–12037.
- 29. Zhu, T.; Yang, Y.; Gong, X. Recent Advancements and Challenges for Low-Toxicity Perovskite Materials. *ACS Appl. Mater. Interfaces* **2020**, *12* (24), 26776–26811.
- Liu, C.-D.; Fan, C.-C.; Liang, B.-D.; Chai, C.-Y.; Jing, C.-Q.; Han, X.-B.; Zhang, W. Spectrally Selective Polarization-Sensitive Photodetection Based on a 1D Lead-Free Hybrid Perovskite Ferroelectric. ACS Mater. Lett. 2023, 5 (7), 1974–1981.
- 31. Li, W.; Xin, D.; Tie, S.; Ren, J.; Dong, S.; Lei, L.; Zheng, X.; Zhao, Y.; Zhang, W.-H. Zero-Dimensional Lead-Free FA₃ Bi₂ I₉ Single Crystals for High-Performance X-Ray Detection. *J. Phys. Chem. Lett.* **2021**, *12* (7), 1778–1785..
- 32. Chen, M.; Dong, X.; Chu, D.; Jia, B.; Zhang, X.; Zhao, Z.; Hao, J.; Zhang, Y.; Feng, J.; Ren, X.; Liang, Y.; Shi, R.; Najar, A.; Liu, Y.; Liu, S. (Frank). Interlayer-Spacing Engineering of Lead-Free Perovskite Single Crystal for High-Performance X-Ray Imaging. Adv. Mater. 2023, 35 (18), 2211977.
- 33. Liu, Y.; Xu, Z.; Yang, Z.; Zhang, Y.; Cui, J.; He, Y.; Ye, H.; Zhao, K.; Sun, H.; Lu, R.; Liu, M.; Kanatzidis, M. G.; Liu, S. (Frank). Inch-Size OD-Structured Lead-Free Perovskite Single Crystals for Highly Sensitive Stable X-Ray Imaging. *Matter* 2020, 3 (1), 180–196.
- 34. Tie, S.; Zhao, W.; Xin, D.; Zhang, M.; Long, J.; Chen, Q.; Zheng, X.; Zhu, J.; Zhang, W. Robust Fabrication of Hybrid Lead-Free

- Perovskite Pellets for Stable X-ray Detectors with Jaw Detection Limit. Adv. Mater. **2020**, 32 (\$\Pi\); 200138\P.5\IO1797A
- 35. Chen, X.; Jia, M.; Xu, W.; Pan, G.; Zhu, J.; Tian, Y.; Wu, D.; Li, X.; Shi, Z. Recent Progress and Challenges of Bismuth-Based Halide Perovskites for Emerging Optoelectronic Applications. *Adv. Opt. Mater.* **2023**, *11* (3), 2202153.
- Xiao, Z.; Meng, W.; Wang, J.; Yan, Y. Thermodynamic Stability and Defect Chemistry of Bismuth-Based Lead-Free Double Perovskites. ChemSusChem 2016, 9 (18), 2628–2633.
- 37. Leng, M.; Yang, Y.; Zeng, K.; Chen, Z.; Tan, Z.; Li, S.; Li, J.; Xu, B.; Li, D.; Hautzinger, M. P.; Fu, Y.; Zhai, T.; Xu, L.; Niu, G.; Jin, S.; Tang, J. All-Inorganic Bismuth-Based Perovskite Quantum Dots with Bright Blue Photoluminescence and Excellent Stability. Adv. Funct. Mater. 2018, 28 (1), 1704446.
- 38. Guo, W.; Xu, H.; Weng, W.; Tang, L.; Ma, Y.; Liu, Y.; Hua, L.; Wang, B.; Luo, J.; Sun, Z. Broadband Photoresponses from Ultraviolet to Near Infrared (II) Region through Light induced Pyroelectric Effects in a Hybrid Perovskite. *Angew. Chem. Int. Ed.* 2022, 61 (52), e202213477.
- 39. Tang, L.; Han, S.; Ma, Y.; Liu, Y.; Hua, L.; Xu, H.; Guo, W.; Wang, B.; Sun, Z.; Luo, J. Giant Near-Room-Temperature Pyroelectric Figures-of-Merit Originating from Unusual Dielectric Bistability of Two-Dimensional Perovskite Ferroelectric Crystals. Chem. Mater. 2022, 34 (19), 8898–8904.
- Ye, H.; Peng, Y.; Shang, X.; Li, L.; Yao, Y.; Zhang, X.; Zhu, T.; Liu, X.; Chen, X.; Luo, J. Self-Powered Visible Infrared Polarization Photodetection Driven by Ferroelectric Photovoltaic Effect in a Dion-Jacobson Hybrid Perovskite. Adv. Funct. Mater. 2022, 32 (24), 2200223.
- Bune, A. V.; Fridkin, V. M.; Ducharme, S.; Blinov, L. M.; Palto, S. P.; Sorokin, A. V.; Yudin, S. G.; Zlatkin, A. Two-Dimensional Ferroelectric Films. *Nature* 1998, 391 (6670), 874–877.
- Haertling, G. H. Ferroelectric Ceramics: History and Technology. J. Am. Ceram. Soc. 1999, 82 (4), 797–818.
- 43. Basu, S. R.; Martin, L. W.; Chu, Y. H.; Gajek, M.; Ramesh, R.; Rai, R. C.; Xu, X.; Musfeldt, J. L. Photoconductivity in BiFeO3 Thin Films. *Appl. Phys. Lett.* **2008**, *92* (9), 091905.
- 44. Ye, H.; Liao, W.; Hu, C.; Zhang, Y.; You, Y.; Mao, J.; Li, P.; Xiong, R. Bandgap Engineering of Lead-Halide Perovskite-Type Ferroelectrics. *Adv. Mater.* **2016**, *28* (13), 2579–2586.
- 45. Liao, W.-Q.; Zhang, Y.; Hu, C.-L.; Mao, J.-G.; Ye, H.-Y.; Li, P.-F.; Huang, S. D.; Xiong, R.-G. A Lead-Halide Perovskite Molecular Ferroelectric Semiconductor. *Nat. Commun.* **2015**, *6* (1), 7338.
- 46. Sun, Z.; Zeb, A.; Liu, S.; Ji, C.; Khan, T.; Li, L.; Hong, M.; Luo, J. Exploring a Lead-free Semiconducting Hybrid Ferroelectric with a Zero-Dimensional Perovskite-like Structure. *Angew. Chem.* 2016, 128 (39), 12033–12037.
- 47. Xiong, R.-G.; Fu, D.-W.; Zhang, Y. Applications of Curie Symmetry Principle in Molecular Ferroelectrics. *Acta Cryst. A* **2017**, *73* (a2), C33–C33.
- Suzuki, K.; Kijima, K. Optical Band Gap of Barium Titanate Nanoparticles Prepared by RF-Plasma Chemical Vapor Deposition. *Jpn. J. Appl. Phys.* 2005, 44 (4R), 2081.
- 49. Wang, L.; Zhang, F.; Chen, C.; He, X.; Boda, M. A.; Yao, K.; Yi, Z. Bandgap Engineering of BZT-BCT by Mn Doping and the

ARTICLE Journal Name

Emerging Strong Photo-Pyroelectric Effect. *Nano Energy* **2024**, *119*, 109081.

- 50. Felix, P.; Gamot, P.; Lacheau, P.; Raverdy, Y. Pyroelectric, Dielectric and Thermal Properties of TGS, DTGS and TGFB. *Ferroelectrics* **1977**, *17* (1), 543–551.
- Sharma, M.; Singh, V. P.; Singh, S.; Azad, P.; Ilahi, B.; Madhar, N.
 A. Porous Ba_{0.85}Ca_{0.15}Zr_{0.1}Ti_{0.9}O₃ Ceramics for Pyroelectric Applications. *J. Electron. Mater.* 2018, 47 (8), 4882–4891.
- Estrada-Vazquez, H.; Webster, R. T.; Das, P. Transverse-Acoustoelectric-Voltage (TAV) Spectroscopy of High-Resistivity GaAs. J. Appl. Phys. 1979, 50 (7), 4913–4919.
- 53. Zhao, C.; Lai, X.; Liu, D.; Guo, X.; Tian, J.; Dong, Z.; Luo, S.; Zhou, D.; Jiang, L.; Huang, R.; He, M. Molecular-Dipole Oriented Universal Growth of Conjugated Polymers into Semiconducting Single-Crystal Thin Films. *Nat. Commun.* 2025, 16 (1), 1509.

View Article Online DOI: 10.1039/D5QI01797A

Open Access Article. Published on 17 2025. Downloaded on 18.10.25 10:18:55.

No This article is licensed under a Creative Commons Attribution-NonCommercial 3.0 Unported Licence.

The data that support the findings of this study are available on request from the corresponding / D5QI01797A author, [Zhihua Sun] , upon reasonable request.